Springer

Numerical study on the characteristics of temperature distribution in continuous welded rail by solar radiation and rail orientation

Sang Hyeon Han[1], Su Ha Hwang[2], Hong Jip Kim[3], Seong J. Cho[3] and Nam Hyoung Lim[4]

[1]Department of Mechanical Engineering, Graduated School, Chungnam National University, Chungnam, Korea, [2]Defense Agency for Technology and Quality, Gyeongnam, Korea, [3]School of Mechanical Engineering, Chungnam National University, Chungnam, Korea, [4]Department of Civil Engineering, Chungnam National University, Chungnam, Korea

Abstract   In summer, the high ambient air temperatures and increased solar radiation cause rises in rail temperatures, and rails can experience the buckling. In this study, a thermo-fluidic analysis was conducted to predict the temperature of a rail. Numerical simulations were performed by changing the orientation of the rails. The south-north rail and the east-west rail was named "0° rail" and "90° rail", respectively. The numerical results from the 0° and 90° rails were validated by comparing them with measured values. Based on this validation, the temperature distribution of a 45° rail was analyzed. The total amount of energies received by the rail were in the order of 0° > 45° > 90°. The results of this study showed that the temperature of a rail can be sufficiently predicted through numerical simulation, and this approach can be used in a forecast to predict a time when buckling might occur.

1. Introduction

Owing to the nature of continuous welded rails (CWRs), it is very important to measure rail temperatures for safe train operation. There are two types of rails: CWRs and standard-length rails (SLRs). The SLR is a rail with a standard length, and a track consisting solely of SLRs will produce a joint between the rails. The noises and vibrations in trains caused by joints are the main causes of damage to the vehicle and track, leading to increased maintenance costs, and making passengers uncomfortable. To overcome these problems, CWRs are widely used, especially for high-speed trains. The CWR is a key technology used in the construction of high-speed rails and is continuously welded with SLRs to remove joints [1, 2].

The main problem with CWRs is that the compressions and expansions caused by temperature changes should be suppressed, as an axial force owing to each temperature change is generated on the rail. Axial forces occur when the rail temperature is different from the rail neutral temperature (RNT). If the rail temperature is higher than the RNT, a compressive force is generated, and if the rail temperature is lower, a tensile force is generated [3, 4]. Excessive compressive and tensile forces result in the fracture or buckling of the track or the breaking of the rail, causing significant problems for train operation. In countries such as the United States, United Kingdom, Australia, and Korea, the safe operating speed is determined by giving the train a speed limit based on the temperature of the rail [5]. Therefore, it is important to predict the temperature of the rail to prevent buckling and breaking in advance. In this study, we focus on the buckling of rails caused by high rail temperatures in summer in Korea.

Rail temperature is an essential parameter for predicting the buckling of a rail. As the temperature of a rail varies with location, a representative measurement point (RMP) is required for monitoring the temperature of the rail. Hong et al. reported a new point for measuring this representative rail temperature, by considering the average deformation of the rail through a struc-

tural analysis adopting experimental and actual rail temperature data [6]. In addition, studies have used probabilistic approaches to predict the buckling of rails, and investigations have been conducted to determine a model for forecasting daily railway weather based on real-time temperature data measured from the soffit of the rail [5, 7]. However, the actual measurement of rail temperature which requires considerable time and cost was necessary in the previous studies. Moreover, the temperature of the rails varies depending on the orientation in spite of the same climatic conditions and corresponding studies were insufficiently done to elucidate this behavior. To overcome these problems, we developed a basic model to predict the temperature of the rails receiving solar radiation using the solar radiation model to simulate the sun, which has been successfully predicted the temperature inside the greenhouse and analyzes the system performance of the solar chimney power plant [8, 9].

The purpose of this study is to develop a numerical model that can predict the temperature of the rail's RMP to prevent rail buckling preemptively. Seasonal and weather conditions that are most likely to cause buckling of the rails were selected in present developed model, and temperature and solar radiation characteristics received by the rails were analyzed by changing the orientation of the rails. A transient analysis was performed to analyze the variation of the rail temperature and solar radiation characteristics according to the change of time from 8:00 to 19:00. In addition, the relationship between the RMP and the nearest outer measurement point to the RMP was investigated. In Sec. 2, a detailed description of the measurement systems and data used in the numerical validation was provided with a detailed description of the governing equations and corresponding modeling. In Sec. 3, the analysis of the numerical results according to the rail orientation was described, and the conclusions of this study were summarized in Sec. 4.

2. Analysis method

2.1 Experimental data for numerical analysis

In this study, we measured climate and temperature data by constructing a measurement system and using an actual rail for the validation of numerical simulations. The rail used for the measurement was UIC 60 cut to a 500 mm length and was installed in east-west and north-south orientations. In addition, the rail was painted black to prevent rust and oxidation. Fig. 1(a) shows the measurement system. Weather stations (Vantage Pro2, Davis) were used to measure the climate data (wind speed, wind direction, temperature, humidity, rainfall, and solar radiation). The rail temperature was measured using thermocouples attached to the inside of the rail. The climate data and rail temperatures were simultaneously transferred to a connected data acquisition system, and the data were stored every 10 min [10]. Fig. 1(b) is a photograph of the installed measurement equipment and rails.

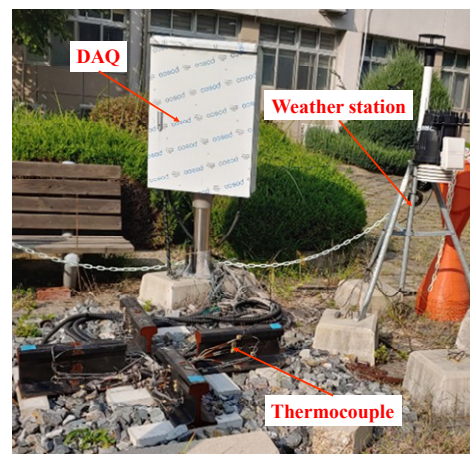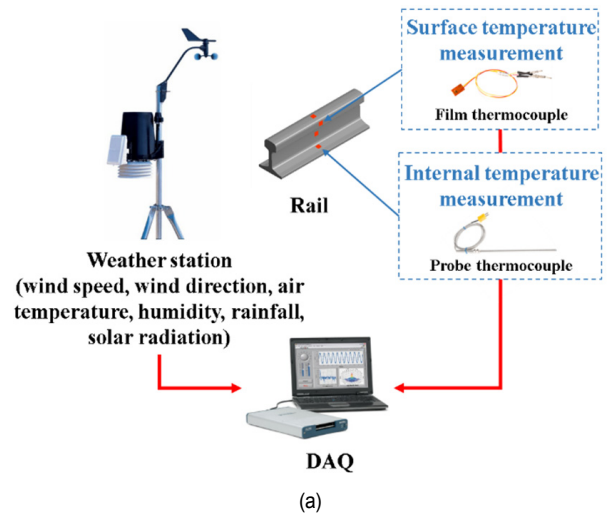The positions of the temperature sensors for the local tem-

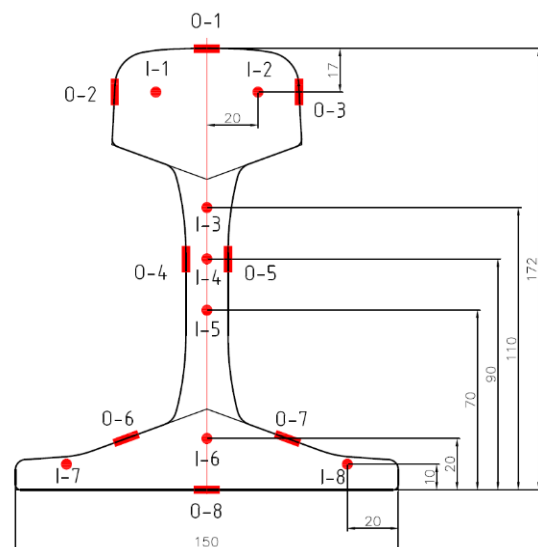Fig. 1. (a) Schematic diagram; (b) installed measurement system for the present study.

Fig. 2. Monitoring points for the temperature measurement in the present rail (I-1 to 8, and O-1 to 8 for inner and outer surface, respectively).
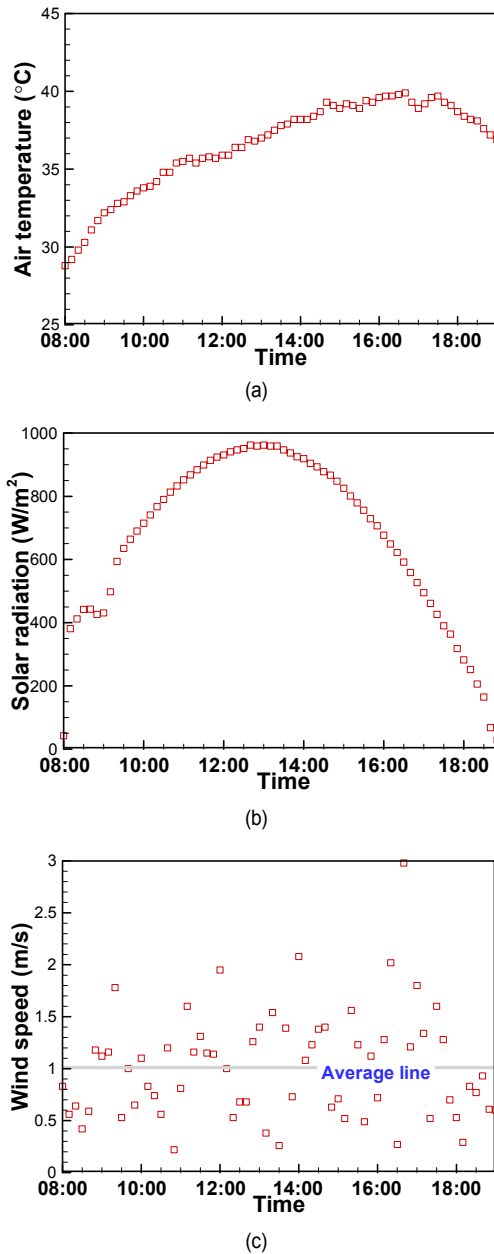
Fig. 3. Climate data such as (a) air temperature; (b) solar radiation; (c) wind speed measured on August 1, 2018.

perature measurement of the rail are shown in Fig. 2. The measured rail temperatures and climate data near the rail were used for numerical validation. The dataset used for the validation of the numerical simulations was measured on August 1, 2018 in Korea. The reasons for selecting this day for the measurement values were as follows. (1) It was a very hot day, with an average temperature of 36.5 °C and a high of 39.9 °C. (2) The weather was clear with few clouds. (3) The average wind speed was 1 m/s, with relatively weak winds. These three conditions were considered to have the most potential for the buckling of the rail. Fig. 3 shows the corresponding weather data.

2.2 Governing equations

The coordinate system introduced for the numerical analysis of the rail is an orthogonal Cartesian coordinate system in which the width direction of the rail is x, the length direction of the rail is z, and the direction opposite gravity is y. It is assumed that in a steady state, an incompressible laminar flow flows around the rail. In addition, solar radiation was included by using a discrete ordinate (DO) radiation model.

The continuity equation can be expressed as shown in Eq. (1) below, where ρ is the density, and $\vec{v}$ is the velocity vector.

$$\frac{\partial \rho}{\partial t} + \nabla \cdot (\rho \vec{v}) = 0 . \tag{1}$$

The moment equation can be expressed as shown in Eq. (2) below, where p is the static pressure, and $\rho \vec{g}$ is a term representing the force owing to gravity.

$$\frac{\partial}{\partial t}(\rho \vec{v}) + \nabla \cdot (\rho \vec{v} \vec{v}) = -\nabla p + \rho \vec{g} . \tag{2}$$

The energy equation can be expressed as in Eq. (3) below. The two terms, bounded by the gradient on the right side, represent the energy transfers via conduction and viscous dissipation, respectively. S_r is the radiation source term. The energy E, used for the motion of the fluid in Eq. (3), is expressed as shown in Eq. (4).

$$\frac{\partial}{\partial t}(\rho E) + \nabla \cdot (\vec{v}(\rho E + p)) = \nabla \cdot (k \nabla T + (\overline{\overline{\tau}} \cdot \vec{v})) + S_r \tag{3}$$

$$E = h - \frac{p}{\rho} + \frac{v^2}{2} . \tag{4}$$

DO model is a method for calculating the radiative transfer equation (RTE) by discretizing space with finite solid angle. Despite requiring much computation time, the DO model can be applied to all radiation problems and has the highest accuracy [11]. In present study, we want to consider not only surface to surface radiation that occurs on solid surfaces but also the radiative effects of humidity. The average relative humidity in summer in Korea is about 74 %, which is very humid. Therefore, RTE as shown in Eq. (5) is adopted to include the radiation effect of humidity.

$$\nabla \cdot (I(\vec{r}, \vec{s})\vec{s}) + (a + \sigma_s)I(\vec{r}, \vec{s})$$
$$= an^2 \frac{\sigma T^4}{\pi} + \frac{\sigma_s}{4\pi} \int_0^{4\pi} I(\vec{r}, \vec{s}')\Phi(\vec{s} \cdot \vec{s}')d\Omega' . \tag{5}$$

Here, $\vec{r}$, $\vec{s}$, and $\vec{s}'$ are the position vector, direction vector, and scattering direction vector, respectively. In addition, a, n, σ_s, σ, I, Φ, and Ω' are the absorption coefficient, refractive index, scattering coefficient, Stefan-Boltzmann con-
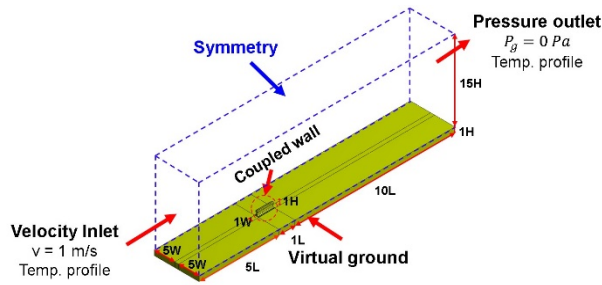
Fig. 4. Geometric domain and boundary conditions used in present numerical simulations.

stant, radiation intensity, phase function, and solid angle, respectively. The scattering coefficient, absorption coefficient, and refractive index are assumed independent of wavelength, and the values are 0 m^{-1}, 0.6 m^{-1}, and 1, respectively. The scattering coefficient was set to 0 m^{-1} because it has O(10^{-4}) m^{-1} according to Ref. [12]. The absorption coefficient was obtained through averaging the data of the experimental absorption coefficient vs. frequency for ambient air with 70.84 % relative humidity in Ref. [13]. Consequently, the absorption coefficient was used as a representative value (0.6 m^{-1}). In addition, since the refractive index of air is 1.0003, it was simplified to 1.

2.3 Rail modeling

A UIC 60 rail was modeled for the numerical analysis of the rail. As can be seen in Fig. 4, the rail was laid on the ground, and the atmosphere was modeled over the ground. As the rail was modeled as 1 W × 1 L × 1 H, the overall domain is modelled as 11 W × 16 L × 16 H, as shown in Fig. 4. The detailed modeling and meshing of the rail and ambient air are shown in Fig. 5. Fig. 5(a) shows the geometry and mesh of the modeled rail, and Fig. 5(b) shows the mesh of the ambient air with the entire domain cut in half, and the rail removed. In order to determine the total number of grids in the computational domain, the grid dependency test of 4 cases (about 1.2, 2.2, 3.7, and 5.4 million) were performed. As a result, the variation of mean temperature between 3.7 and 5.4 million grids showed almost the same behaviors with the difference of less than 0.1 K. Therefore, all numerical simulations were performed with 3.7 million grids. The ambient air surrounding the rail was meshed using structured grids to reduce the overall calculation time and improve the accuracy of the analysis results.

2.4 Boundary conditions

The overall boundary conditions are shown in Fig. 4. The inlet conditions were set as a velocity inlet with an average wind speed of 1 m/s, and the temperature profile shown in Fig. 3(a) was applied. The outlet simulated the opening conditions by setting the gauge pressure to zero, and to the same temperature profile as Fig. 3(a) as the entrance conditions were applied. The other sides of the ambient air (except for the inlet and out-
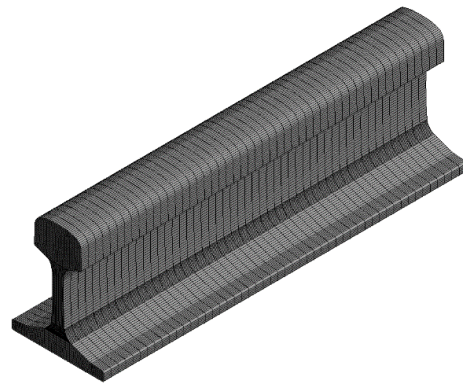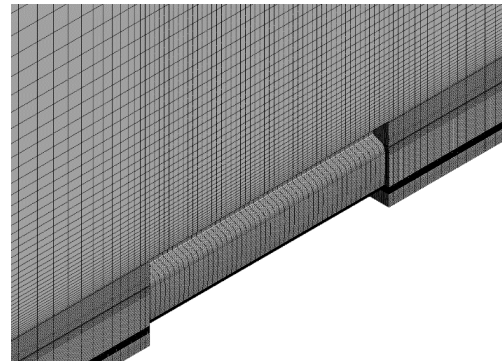
Fig. 5. Grid distribution of (a) the present rail; (b) ambient air.

let) were subjected to a symmetry condition, so that any other flows could not affect the rail. The interface between the ambient air and rail was set as a coupled wall, to allow heat transfer between the two. The ground was simulated as a virtual wall condition to allow heat transfer between the rail and the ground, and the depth was set to 1H. The rail specimen used in the experiment was painted black to prevent rust and oxidation, and the surface absorptivity of black is generally known as 0.8~0.9. The absorptivity was set to 0.8 in consideration of dust and other foreign substances accumulated on the surface of the rail specimen. In addition, since the absorptivity of the gray surface is known as 0.4~0.5, so the absorptivity of the ground was set to 0.4.

2.5 Solar radiation model

In ANSYS FLUENT software, solar load models can be used to calculate the radiation effects from the sun's rays entering a computational domain. Two options are available for the model: solar ray tracing and DO irradiation. In this study, solar ray tracing was used. Solar ray tracing method is used to predict the direct illumination energy source due to incident solar radiation coming from outside the computational domain. The computational domain can be divided into 3 parts which consist of ground, rail, and ambient air. The solar ray reaches the boundary surfaces of the ground and rail domain after passing

through the ambient air. In the ambient domain, RTE of ambient air with humidity is calculated, and shading analysis is applied in the ground and rail domain. Shading analysis determines shadows on boundary faces and interior walls and calculates the heat flux of boundary faces due to incident radiation. The calculated heat flux is added as the source term of the energy equation.

Solar irradiation includes direct beam solar irradiation and diffuse solar irradiation, and the sum of these two components is called global irradiation. The solar ray tracing uses both a positioning vector for the solar location and two illumination parameters to represent solar load. To specify the magnitude and direction of the sun, the solar calculator can be used. The solar calculator needs specifications of the coordinates at which the model is located, date and time of day to calculate the sun vector and the magnitudes of the illumination parameters. The combination of these parameters gives a solar ray that would appear at this certain location in the world at that given time. Two illumination parameters used to describe the intensity of the solar load consist of two irradiation terms, direct solar irradiation and diffuse solar irradiation [11]. The approximate values of direct solar irradiation and diffuse solar irradiation calculated by solar calculator utility in this study are 80 to 90 % and 10 to 20 % of global irradiation, respectively.

In this study, the solar calculator was set as follows. The longitude, latitude, and time zone were set as 127, 37, and 9, respectively, corresponding to the location of the measurement system in Korea. The date was set to August 1; this date was considered to have a high probability of rail buckling. The start time was set to 8 o'clock, and buildings around the measurement system created no shadows.

2.6 Ground conditions

An actual track has track ballast around railway sleepers. The rail is fixed to the sleepers, which are made of concrete. The ballast distributes the load on the sleeper and prevents the rail from stretching by fixing the sleeper with the ballast's resistance. Part of the actual rail soffit is in contact with the concrete sleepers, and the rest is in contact with the ballast, creating voids. To completely model the ground of actual rails, we need to model the sleepers and gravel, to show the convection effect into the gravel gap. However, this method is practically difficult. Therefore, in this study, the ground is simplified to a cubic shape, by applying a virtual wall condition.

However, simplifying the ground into a cubical shape causes two problems, as follows. (1) The rail soffit and the ground make perfect contact. (2) The convection effects between gravels cannot be included. To overcome these two problems, we arbitrarily changed the properties of the ground (thermal conductivity, density, and specific heat), and found the approximate properties that were the most similar to the actual conditions. For example, only the average temperature of the rail was considered, and the approximate properties were found by changing the properties until a similar result was ob-

tained. Then, the approximate properties were determined by comparing the local temperatures of the head and base of the rail.

Based on the approximate properties obtained in this way, two cases (north-south rail and east-west rail) were investigated and showed satisfactory agreement with the local temperatures obtained through measurement. Therefore, the approximate ground properties were thought to be reliable. Consequently, the applied properties for the ground conditions were as follows: the thermal conductivity $k = 0.36 \, \text{W}/\text{mK}$, density $\rho = 1840 \, \text{kg}/\text{m}^3$, and specific heat $C_P = 2500 \, \text{J}/\text{kgK}$.

3. Results and discussions

The representative climate factors affecting rail temperatures include the air temperature, humidity, solar radiation, and wind speed. Through a correlation analysis [14] with these four factors and the rail temperature, it has been determined that the wind speed has a very low coefficient of correlation with the rail temperature. Based on this analysis, the numerical results of this study assume that the wind blows in the longitudinal direction of the rail, regardless of the rail orientation. In addition, the inclined angle of the track for high speed train is neglected because it is very small (maximum 35 mm per 1 km), in general.

The orientation of the rail is expressed in degrees, by rotating counterclockwise with respect to the south-north rail (0° rail). Therefore, the south-east rail and the east-west rail are denoted as the 45° and 90° rails, respectively, as shown in Fig. 6(a). Fig. 6(b) shows the locations of the rails in the measurement system and the path of the sun, considering the geological features of the summer in Korea. Owing to the complexity of the rail geometry, the solar radiation area received by the rail depends on the orientation of the rail. Accordingly, the local temperatures of the rail will be different. This paper describes the trends of the rail temperature and solar radiation according to the rail orientation.

3.1 0° rail

Figs. 7 and 8 show the behavior of inner and outer temperature among the monitoring points of the 0° rail, respectively, with the highest temperatures at I-2 and O-1, and with the lowest temperatures at I-3 and O-2. The location of these points can be found in Fig. 2. Fig. 9 shows the mean temperature, solar radiative heat of the 0° rail, and corresponding cross-sectional contour of the rail, representing the temperature distribution at the indicated time. Each contour is set to a different range of legends to more clearly illustrate the temperature distribution. At 10:00, the right side of the rail base showed the highest temperature, and at 13:00, the temperatures on the left side of the rail head and base were high. At 16:00, the temperature on the left side of the rail base was the highest, and at 19:00, the temperature on the rail web was high.

For the 0° rail, the sun rises and falls in a direction perpen-

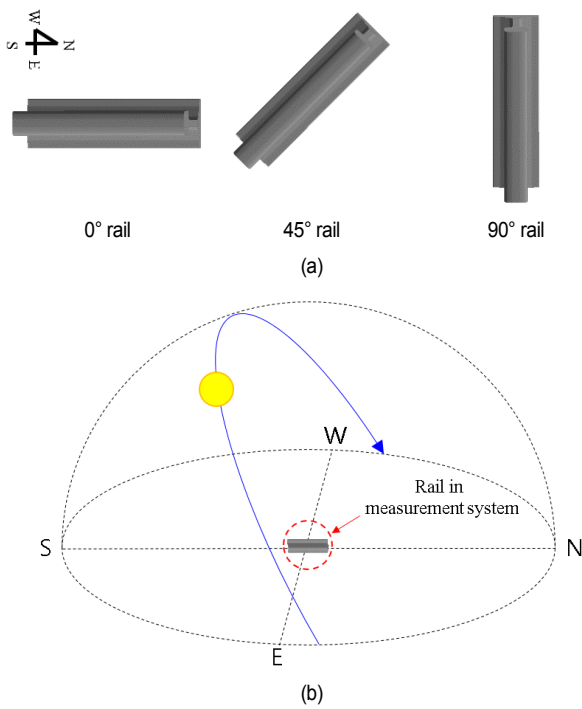0° rail   45° rail   90° rail

(a)

(b)

Fig. 6. (a) Name of the rail expressed in degrees; (b) the path of the sun considering the geological features of the summer in Korea.

dicular to the length of the rail. Thus, depending on the position of the sun, the rail surface mean solar heat flux appears to have two maximum values. This can be easily understood by considering the solar radiation surface area received by the rail. In the case of August 1, which is considered in this study, the surface area of the rail receiving solar radiation formed on the east side at approximately 8 a.m., and this surface area gradually increased over time. The maximum value of the rail surface area affected by the solar radiation appeared at approximately 10:30. After that, the rail surface area decreased until approximately 11:50. Subsequently, the rail surface area affected by the solar radiation remained nearly constant from 11:50 to 13:30, increased again after approximately 13:30, and then had a maximum value at approximately 15:00 before continuing downwards.

These characteristics of the solar radiation heat flux received by the rail surface also affect the temperature of the rail. In general, the amount of solar radiation in summer has a large influence on the temperature of the rail. Therefore, the tendency of the rail temperature is influenced by the amount of solar radiation the rail surface receives, resulting in a section in which the temperature gradient decreases over time, and then increases again. In this study, the focus was not only on making a model that could accurately predict the temperature of a
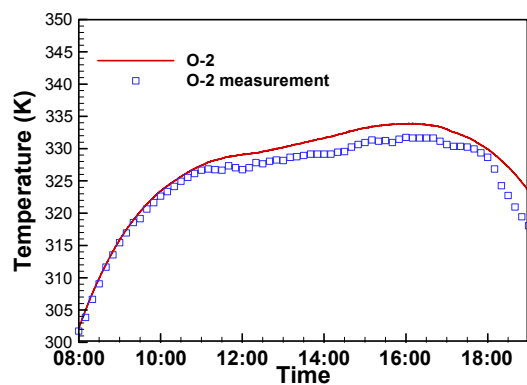

(a)
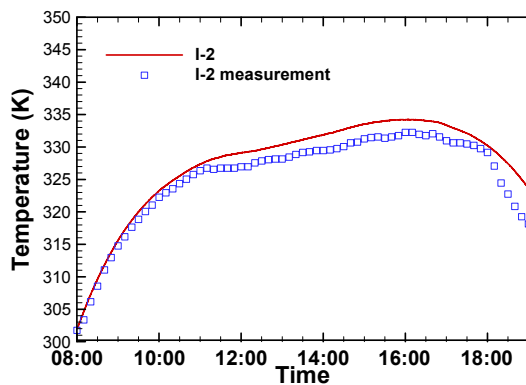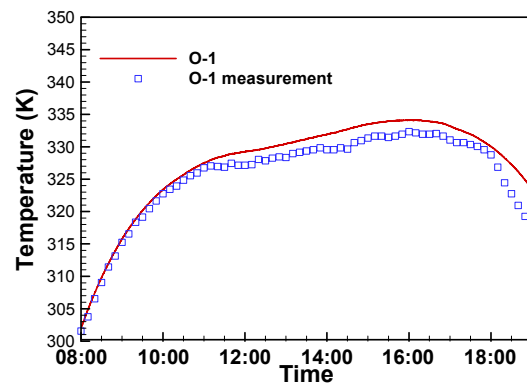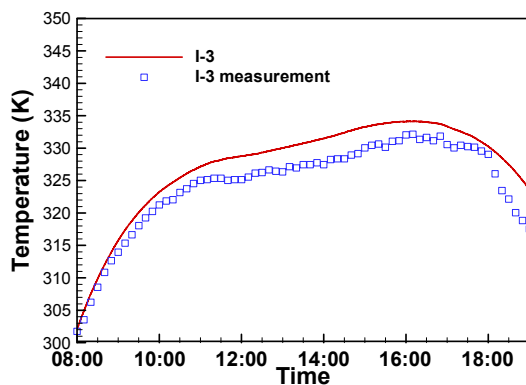
(b)

Fig. 7. Inner temperature of 0° rail: (a) the highest (I-2); (b) the lowest point (I-3).

(a)

(b)

Fig. 8. Outer temperature of 0° rail: (a) the highest (O-1); (b) the lowest point (O-2).

rail by numerical simulation, but also on predicting the tendency. The temperatures calculated by the present simulation show that the characteristics of the temperature variations at each location show satisfactory agreement with the experimental data.
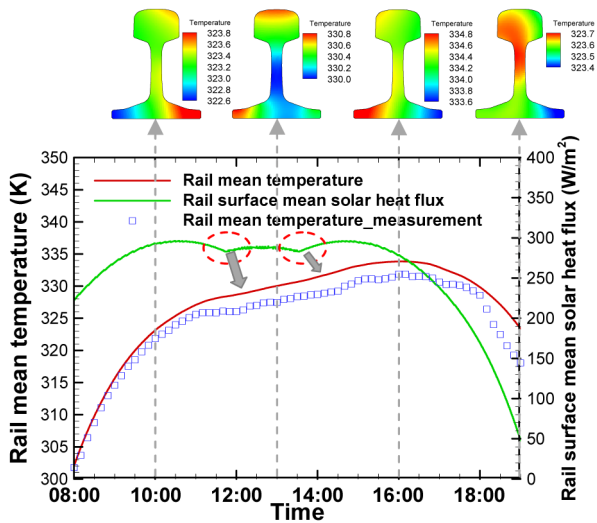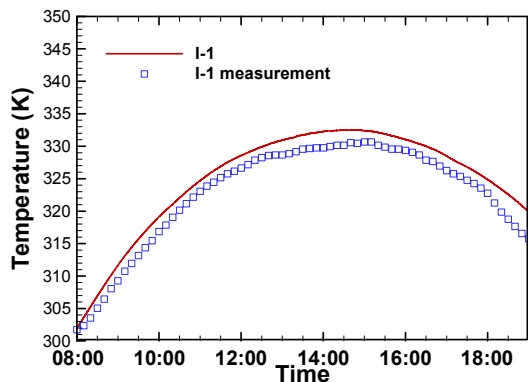

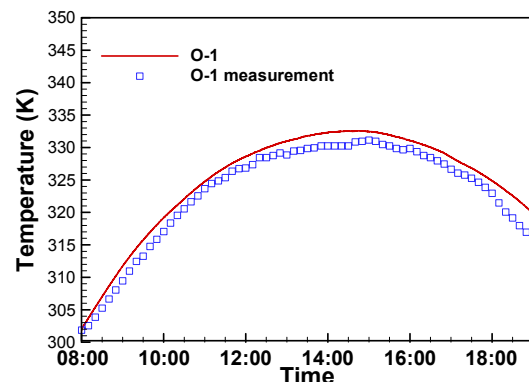Fig. 9. Mean temperature and surface mean solar heat flux of 0° rail.

3.2 90° rail

Similar to the results of 0° rail, Figs. 10 and 11 show the behavior of inner and outer temperature, respectively, with the highest temperatures at I-1 and O-1, respectively, and with the lowest temperatures at I-8 and O-4, respectively among the monitoring points of the 90° rail. Fig. 12 shows the mean temperature and solar radiative heat of the 90° rail, and the corresponding cross-sectional contour of the rail, representing the temperature distribution at the indicated time. At 9:00, the left side of the rail base showed the highest temperatures, and at 12:00 and 15:00, the left side of the rail head and base had the highest temperatures. At 19:00, the temperature on the right side of the rail base was the highest.

In the case of the 90° rail, the sun rises and falls through the longitudinal direction of the rail. Unlike the 0° rail, the surface area of the 90° rail that absorbs the solar radiative heat does not dramatically increase or decrease over time. Consequently, the mean solar heat flux shows a quadratic behavior with only one local maximum value at the highest altitude of the sun, at approximately 12:30. This is easily understood by considering the surface area of the solar radiation that the rail receives over time. Therefore, the mean temperature of the rail also shows a certain quadratic behavior (similar to that of the mean solar
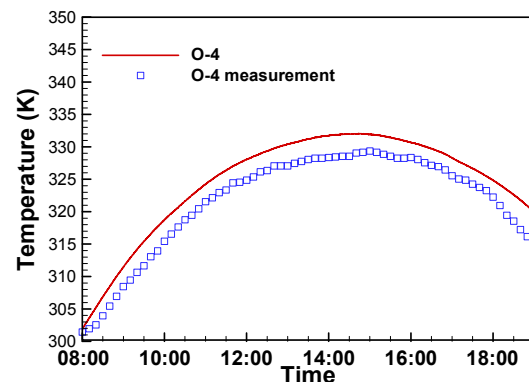

(a)
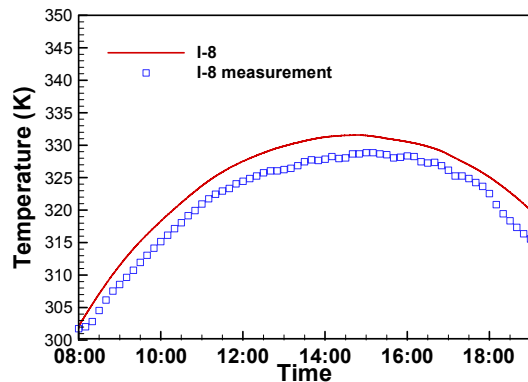
(b)

Fig. 10. Inner temperature of 90° rail: (a) the highest (I-1); (b) the lowest point (I-8).

(a)

(b)

Fig. 11. Outer temperature of 90° rail: (a) the highest (O-1); (b) the lowest point (O-4).
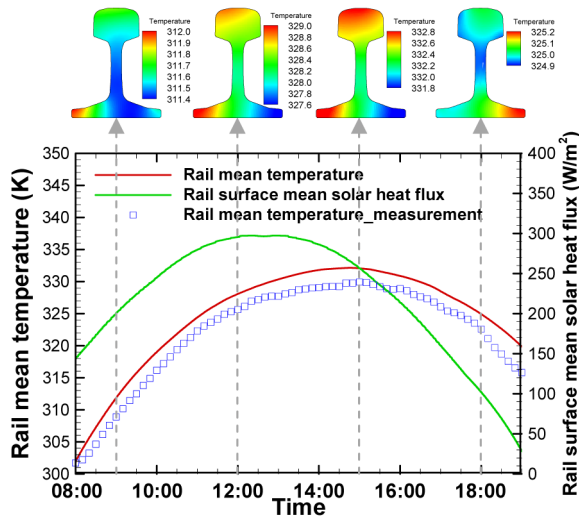
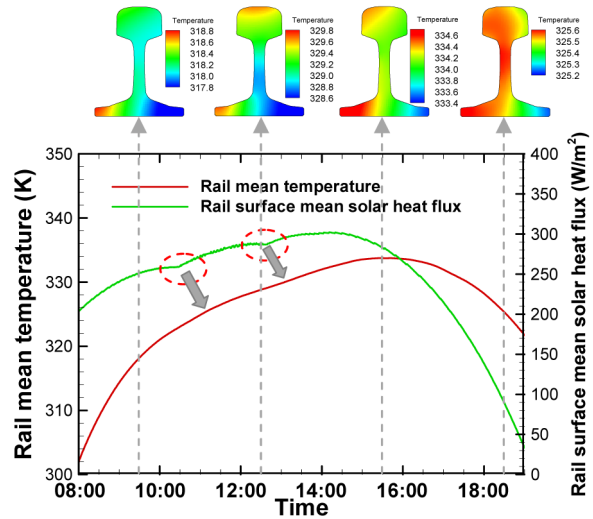Fig. 12. Mean temperature and surface mean solar heat flux of 90° rail.

Fig. 13. Mean temperature and surface mean solar heat flux of 45° rail.

heat flux), which is thought to be mainly affected by the absorbed solar radiative heat.

Although the numerical simulation conditions used in this study cannot predict the temperature of all rails in different environments, the numerical simulation results for the 0° and 90° rails at the current measuring locations show that computational fluid dynamics can (potentially) sufficiently predict the temperature distribution of an actual rail.

3.3 45° rail

Based on the numerical simulation results for the 0° and 90° rails, the rail temperature appears to be mainly affected by the solar radiative heat flux, and the view factor between the rail and the sun. To confirm this observation, a numerical simulation was conducted for the 45° rail. Although there are not any available measured data, the numerical results for the 0° and 90° rails indicate that the rail temperature can be sufficiently predicted.

Fig. 13 shows the mean temperature and solar radiative heat of the 45° rail and the corresponding cross-sectional contour of the rail, representing the temperature distribution at the indicated time. At 9:30, the left side of the rail base showed the highest temperature, and at 12:30, the temperatures of the left side of the rail head and base were high. At 15:30, the temperature on the left side of the rail base was the highest, and at 18:30, the left side of the rail had the highest overall temperature.

The average amount of solar radiation received by a rail surface shows two points appearing at approximately 10:30 and 12:30, at which the gradient suddenly changes, owing to the view factor between the rail and sun. The average solar radiation received by the rail surface gradually increases from 8:00, peaks at approximately 14:30, and then decreases rapidly. The temperature of the rail has a section where the gradient decreases and then increases (similar to the case with
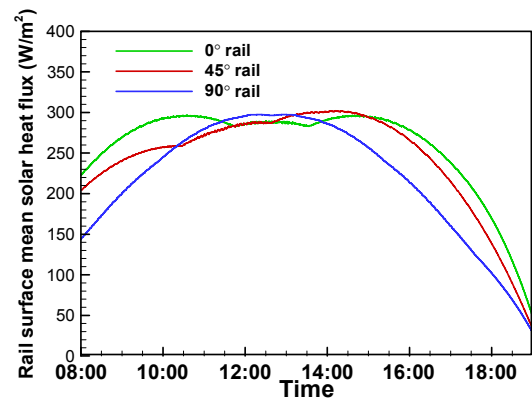

Fig. 14. Comparison of solar heat flux with respect to the rail orientation.

the 0° rail), but it is hard to see with the naked eye. This is because, as compared with the 0° rail, the change in the gradient relative to the average solar radiative heat received by the rail surface is not large enough to affect the temperature change of the rail.

3.4 Effects of rail orientation

Fig. 14 shows a comparison of the mean solar radiation of the rail surfaces with respect to the rail orientation. The total amount of solar radiation received by each rail is the largest for the 0° rail, but between 11:30 and 15:00, there are time periods where the 45° and 90° rails receive slightly more radiation. To illustrate this quantitatively, the total absorbed solar radiative heat Q, defined in Eq. (6), was investigated. In Eq. (6), q is the solar heat flux received by the rail surface.
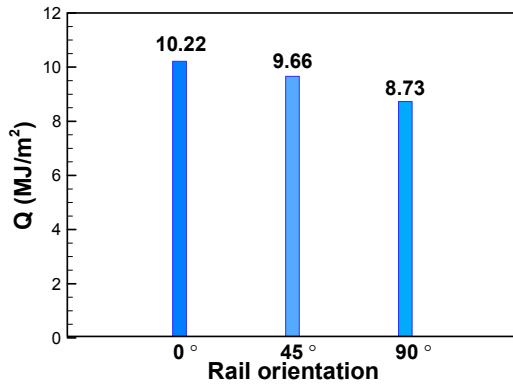
$$Q = \int_0^{\Delta t} q \, dt \,. \tag{6}$$

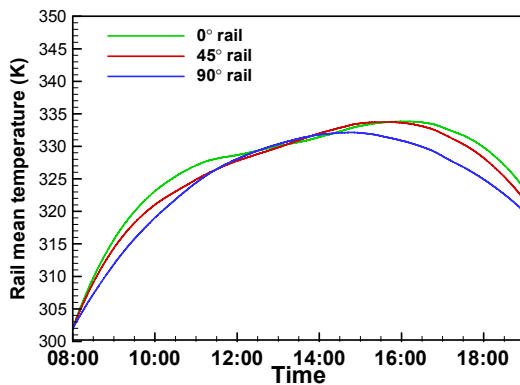Fig. 15. Total energy received by the rails in each orientation.

Fig. 16. Comparison of mean temperature with respect to the rail orientation.

The Q value represents the total amount of energy received by the rail over the entire time. The values of the total energy received by the 0°, 45°, and 90° rails are 10.22 MJ/m^2, 9.66 MJ/m^2, and 8.73 MJ/m^2, respectively, as shown in Fig. 15. It can be seen that as the rail orientation approaches 0°, the total amount of energy received by the rail increases.

Fig. 16 shows the mean temperature along each rail orientation. Because the solar radiation directly affects the temperature of the rail, the 0° rail (with the largest total energy) has the highest temperature distribution, except for in certain time periods. Among the rail temperatures in each orientation, the 0° rail had the steepest temperature gradient in the morning, resulting in a rapid rise in temperature and a gap of more than 4 °C from the temperature of the 90° rail. The 90° rail had the highest temperature at approximately 13:00 but did not differ much from the temperatures of the other rails. In addition, after 14:00, the temperature difference between the 0° and 90° rails was more than 6 °C. The temperature difference between the 0° and 45° rails gradually widens throughout the morning. These rails have a similar section at approximately 12:30 and a similar temperature range, but the temperature difference starts to widen again at approximately 16:00. The maximum temperature of the rail does not occur at the time when the average amount of solar radiation received by the rail surface is the highest. This is because the rail temperature is not immediately
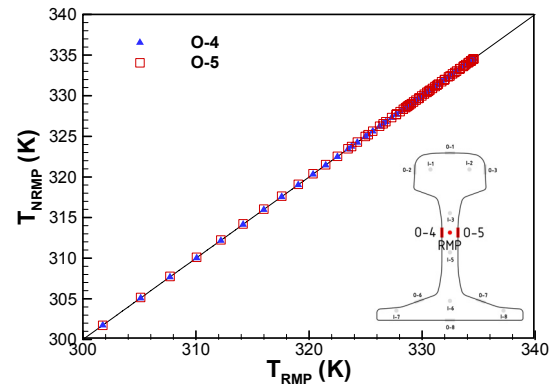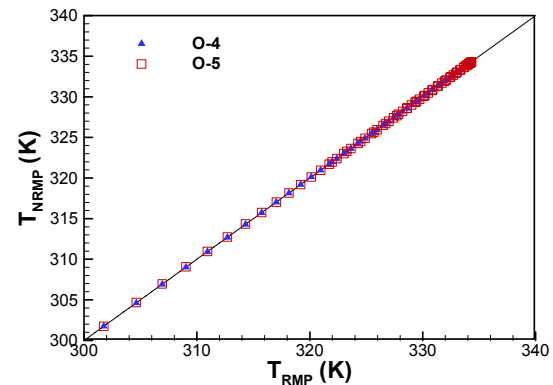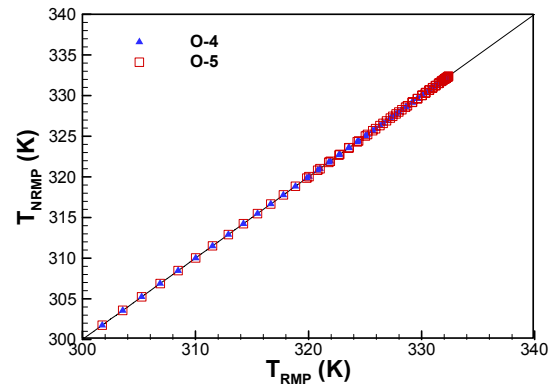
Fig. 17. Relationship between representative measurement point (RMP) and nearest RMP (NRMP) in each rail orientation: (a) 0°; (b) 45°; (c) 90° rail.

affected by the solar radiation; it is affected after a certain amount of time.

The times when the rails have the maximum temperatures are 16:00, 15:30, and 15:00 for the 0°, 45°, and 90° rails, respectively. In the contour corresponding to 16:00 in Fig. 9, the web temperature of the 0° rail is relatively high. This is because the sun is on the left side of the 0° rail at approximately 16:00; therefore, direct solar radiation is delivered to the web. In contrast, for the 90° rail, the temperature of the web appears relatively low (as shown in the contour corresponding to 15:00).

This is because the sun is located at the top of the rail, as shown in Fig. 12. The absolute value of the maximum temperature is predicted in the order of $0° \geq 45° > 90°$, and the maximum temperature of the 0° and 90° rail is 334.3 and 332.5 K, respectively, resulting in a temperature difference of 1.8 K. This indicates that the measurement time should be considered according to the orientation to properly measure the maximum temperature of an actual rail. Moreover, the maximum temperature of the rail does not coincide with the time when the meridian altitude of the sun is highest, but rather after some time delay, owing to the rail's internal heat conduction. These behaviors show that the rail orientation should be carefully included to evaluate the rail temperature properly.

3.5 Representative measurement point (RMP) temperature prediction

As it is difficult to directly measure the temperature of an RMP in an actual rail, a measuring point outside the rail that can represent the temperature of the RMP is required. It was assumed that the temperature at O-4 and 5, i.e., the nearest to the RMP (NRMP), could represent the temperature of the RMP. To confirm this assumption, the relationship between the RMP and NRMP was analyzed, and is shown in Fig. 17. As shown in Fig. 17, a satisfactory agreement was obtained between the RMP and NRMP with coefficient of determination of $R^2 = 0.9999$. Consequently, it is considered possible to predict the temperature of the RMP by measuring the temperature of the NRMP, regardless of rail orientation.

4. Conclusions

Numerical simulations were conducted based on a solar radiation model, to predict the temperature of rails in the summer in Korea. The present results showed satisfactory agreement with previous experimental data. As the surface area of the rail exposed to direct sunlight varies according to the orientation of the rail, a temperature difference occurs for each rail orientation. As the 0° rail was in the orientation of receiving significant direct sunlight, the total amount of energy received by that rail was the highest, and the maximum and overall temperatures of the rail were also high. In contrast, the 90° rail was in the orientation of the least direct sunlight, so the total amount of energy received by the rail was the lowest, and the maximum and overall temperatures of the rail were also low.

By comparing the rail surface mean solar heat flux in each orientation, it can be seen that the 45° rail has different and unique characteristics and does not simply comprise intermediate values of the 0° and 90° rails. In this respect, further consideration of rail orientations for predicting rail temperature distributions in actual conditions is necessary. Consequently, the solar radiation heat and exposed rail surface area with respect to time were the major parameters affecting the temperature distribution of the rail.

Present results can be applied to accurately predict the rep-

resentative rail temperature for preemptive prevention of rail buckling during the hot season. If big data were constructed for various parameters such as the solar radiation heat flux, rail orientation, and weather conditions, a precise prediction of rail temperatures would be possible.

Nomenclature——————————————————

a	: Absorption coefficient
C_P	: Specific heat
g	: Gravity
I	: Radiation intensity
k	: Thermal conductivity
n	: Refractive index
p	: Static pressure
q	: Solar heat flux
Q	: Total absorbed solar radiative heat
$\bar{r}$	: Position vector
$\bar{s}$	: Direction vector
$\bar{s}'$	: Scattering direction vector
$\bar{v}$	: Velocity vector
ρ	: Density of air
σ	: Stefan-Boltzmann constant
σ_s	: Scattering coefficient
Φ	: Phase function
Ω'	: Solid angle

References

[1] A. Kish and G. Samavedam, *Track Buckling Prevention: Theory, Safety Concepts, and Applications*, Report no. DOT/FRA/ORD-13/16, Department of Transportation, Federal Railroad Administration, Washington, USA (2013).

[2] I. N. Martinez, I. V. Sanchis, P. M. Fernandez and R. I. Fraco, Analytical model for predicting the buckling load of continuous welded rail tracks, *Proceedings of the Institution of Mechanical Engineers; Part F: J Rail Rapid Transit*, 229 (5) (2014) 542-552.

[3] A. Kish, R. S. McWilliams and H. Harrison, Track buckling hazard detection and rail stress management, *Proceedings of the 9th World Congress on Railway Research*, Lille, France (2011) 10.

[4] M. A. Van, Buckling analysis of continuous welded rail track, *HERON*, 41 (3) (1996) 175-186.

[5] L. Chapman, J. E. Thornes and Y. Huang, Modelling of rail surface temperatures: a preliminary study, *Theoretical and Applied Climatology*, 92 (2008) 121-131.

[6] S. U. Hong, H. S. Jung, C. Park, H. W. Lee, H. U. Kim, N. H. Lim, H. U. Bae, K. H. Kim, H. J. Kim and S. J. Cho, Prediction

of a representative point for rail temperature measurement considering longitudinal deformation, *Proceedings of the institution of mechanical engineers; Part F: Journal of Rail and Rapid Transit*, 233 (10) (2019) 1003-1011.

[7] A. Kish and G. Samavedam, Risk analysis based CWR track buckling safety evaluations, *Proceedings of International Conference on Innovations in the Design & Assessment of Railway* (1999) 1-19.

[8] G. Tong, D. M. Christopher and B. Li, Numerical modelling of temperature variations in a Chinese solar greenhouse, *Computers and Electronics in Agriculture*, 68 (1) (2009) 129-139.

[9] P. H. Guo, J. Y. Li and Y. Wang, Numerical simulations of solar chimney power plant with radiation model, *Renewable Energy*, 62 (2014) 24-30.

[10] S. U. Hong, H. U. Kim, N. H. Lim, K. H. Kim, H. J. Kim and S. J. Cho, A rail-temperature prediction model considering meteorological conditions and the position of the sun, *International Journal of Precision Engineering and Manufacturing*, 20 (2019) 337-346.

[11] *ANSYS Fluent User's Guide v14.5*, Canonsburg: ANSYS Inc.

[12] G. L. Knestrick, T. H. Cosden and J. A. Curcio, Atmospheric scattering coefficients in the visible and infrared regions, *Journal of the Optical Society of America*, 52 (9) (1962) 1010-1016.

[13] D. M. Slocum, E. J. Slingerland, R. H. Giles and T. M. Goyette, Atmospheric absorption of terahertz radiation and water vapor continuum effects, *Journal of Quantitative Spectroscopy & Radiative Transfer*, 127 (5) (2013) 49-63.

[14] J. Y. Choi, G. S. Lee, H. U. Bae, B. H. Park and N. H. Lim, Investigation on the temperature characteristics of CWR for the climate change, *Journal of the Korean Society for Railway*, 13 (2) (2010) 179-185.

Sang Hyeon Han received his B.S. degree at Department of Mechanical Engineering of Chungnam National University, Korea, in 2019 and is currently in his M.S. degree at Chungnam National University, Korea since 2019. His research interests are in combustion engineering, propulsion system, and fuel cell system.

Su Ha Hwang received his B.S. degree at the Department of Mechanical Engineering at Chungnam National University, Korea, in 2017, and his M.S. degree in 2019. He has worked in the DTaQ (Defense Agency for Technology and Quality) as a junior engineer. His research interests are in combustion engineering, propulsion system, and CFD.
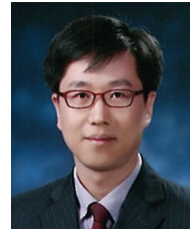
Hong Jip Kim is a Professor at School of Mechanical Engineering of Chungnam National University, Korea. His research interests are in combustion phenomena, thermo-acoustic instability, combustion instabilities in various combustors and propulsion systems.

Seong J. Cho is Associate Professor at School of Mechanical Engineering of Chungnam National University, Korea. His research interests are in advanced sensor system, Nano/micro materials, MEMS/NEMS, advanced fabric, biomedical engineering, biomimetics, and bio-sensor.

Nam Hyoung Lim is a Professor at Department of Civil Engineering of Chungnam National University, Korea. His research interests are in railway and track engineering, steel structure engineering, and structural engineering.